Flow, Turbulence and Combustion
https://doi.org/10.1007/s10494-025-00645-8

RESEARCH

Towards Efficient Hybrid RANS–LES for Industrial Aeronautical Applications

Axel Probst[1] · **Elrawy Soliman**[1] · **Silvia Probst**[1] · **Matthias Orlt**[1] · **Tobias Knopp**[1]

Received: 16 April 2024 / Accepted: 17 February 2025

Abstract

Three complementary approaches for reducing the grid-resolution requirements in hybrid RANS–LES computations, namely (a) the use of wall functions, (b) the application of locally embedded WMLES instead of global WMLES, as well as (c) local grid adaptation in LES regions, are assessed for different test cases up to an industry-relevant aeronautical flow. In this context, targeted improvements and an extension to general 3D geometries of an embedded WMLES method in a second-order accurate, unstructured compressible finite-volume solver are presented. For the wall functions and the embedded WMLES, which are applied to the NASA hump flow and the CRM-HL aircraft configuration, significant computational efficiency gains relative to corresponding reference simulations are demonstrated, while the loss of predictive accuracy compared to experiments can be limited to acceptable levels. Using a refinement indicator based on the locally resolved turbulent kinetic energy, the grid adaptation applied to the NASA hump flow and the NACA0021 at stall conditions yields partly even improved results compared to computations on globally-refined fixed grids, but the computational overhead due to the iterative refinement and averaging process was not yet included in this study. With grid-point savings ranging between 1/3 and more than 2/3 of grid points compared to respective reference meshes, all considered methods offer potential towards more efficient hybrid RANS–LES simulations of complex flows, although their accumulated potential through combination still needs to be explored.

Keywords Hybrid RANS–LES · Wall functions · Embedded wall-modelled LES · Grid adaptation · CRM-HL

1 Introduction

Hybrid RANS–LES methods (HRLM) aim to combine the efficiency of RANS modelling with the accuracy of LES in a localized manner. Variants of the Detached-Eddy Simulation (DES), e.g. Spalart et al. (2006), Shur et al. (2008), have become established tools that are nowadays applied to complex industrial flows, such as full aircraft in high-lift conditions, cf. Ashton et al. (2022), Probst and Melber-Wilkending (2022a). However, the

---

E. Soliman, S. Probst, M. Orlt, and T. Knopp contributed equally to this work.

Extended author information available on the last page of the article large computational effort due to the temporal and spatial resolution of local LES are still a major obstacle for wider application, especially in commercial aeronautical industry, due to the large Reynolds numbers of aircraft in flight.

The goal of accelerating numerical simulations can generally be addressed by more efficient solver algorithms or by increasing the computing resources spent on a given problem size, provided that the parallel-scalability limitations of the numerical solver are not reached, cf. Probst et al. (2020). However, while both aspects are subjects of active research, cf. Jägerskupper and Vollmer (2022), the potential acceleration of unsteady scale-resolving simulation methods faces competing demands and restrictions. For instance, industrial multi-purpose solvers still consider steady-state RANS modelling as standard application and need to be compatible with multi-disciplinary simulation environments.

For this reason, the present investigation concentrates on model-specific efficiency aspects and puts the main focus on the high numerical resolution demands of hybrid RANS–LES. While in LES the required time resolution for an accurate representation of turbulent structures is linked to the grid spacing and is therefore difficult to adjust independently, there are, however, approaches to reduce the overall number of grid points with ideally only little impact on accuracy.

In this work, three such approaches are considered to explore their potential for accelerating DES-type simulations in the framework of a second-order unstructured compressible finite-volume solver, called DLR-TAU, cf. Schwamborn et al. (2008):

(a) *Use of wall functions in order to reduce the wall-normal resolution close to walls.* Bridging the viscous sub-layer via analytical wall laws is a classic approach from steady RANS modelling, which is also now common in certain wall-modelled (or wall-function) LES approaches. Also the combination with hybrid RANS–LES, be it of DES-type, cf. Mockett et al. (2012), Herr and Probst (2021), or other variants of HRLM, cf. Stoellinger et al. (2019), have been demonstrated for fundamental flows. However, their applicability to complex aircraft flow in the framework of hybrid RANS–LES has not yet been fully explored.

(b) *Local grid adaptation in LES regions in order to reduce the resolution compared to fixed, globally-refined LES grids.* Defining suitable indicators for refinement in the framework of DES-type hybrid RANS–LES poses a challenge, since the local grid resolution in LES regions also affects the sub-grid modelling, and not only numerical discretization errors that are typically addressed by adaptation. Moreover, RANS regions should be excluded from the refinement, which can be realized by combining different flow- and modelling quantities with the LES-resolution indicator, cf. Limare et al. (2020).

An overview of quality measures for the local LES resolution is given by Celik et al. (2009). One well-known criterion for well-resolved LES, cf. Pope (2004), which demands at least 80 % of turbulent kinetic energy (TKE) to be resolved, was successfully applied to LES of the flow in a meso-combustor in Benard (2016), but it also was recently challenged by Toosi and Larsson (2020) for its strict locality. Their proposed optimization procedure for the overall grid-size (or filter) distribution shows high potential, but appears difficult to adopt efficiently for complex applications. Therefore, and based on promising first tests on fundamental flows in Reuß et al. (2015), we adopt an implementation of the 80%-TKE criterion as grid-adaptation indicator in a full refinement process and compare it with the “Index of resolution quality” of Celik et al. (2009) in two test cases.

(c) *Embedded wall-modelled LES (EWMLES) using synthetic-turbulence generation (STG) at the prescribed RANS–WMLES interface.* This approach allows restricting WMLES resolution to critical flow areas, e.g. local separations, while applying RANS modelling everywhere else. Thus, especially in flows with a wide range of flow phenomena, large amounts of grid points may be saved compared to a global WMLES. For the synthetic-turbulence generation as a main ingredient of EWMLES, various approaches based on e.g. synthetic turbulent eddies by Jarrin et al. (2009) or superimposed Fourier modes with realistic spectral properties, cf. Shur et al. (2014), have been proposed and successfully applied in hybrid RANS–LES simulations of quasi-2D flows. However, applications to real 3D cases are still rare, e.g. Herr et al. (2023), as these pose additional requirements for the generalizability of the STG method and for the ease of setting up embedded WMLES regions on complex geometries.

To increase the applicability range of such methods, we present an extended implementation of EWMLES for unstructured flow solvers based on IDDES of Shur et al. (2008) and the NTS-STG of Shur et al. (2014), which is rather easy to apply to 3D geometries and provides an improved local source-term injection of the synthetic fluctuations at the RANS–WMLES interface. A demonstration to a full high-lift aircraft configuration enables a first assessment of the method for an industry-relevant aeronautical flow.

After a brief outline of the numerical method and the basic hybrid modelling in Sect. 2, the three mentioned approaches for improved efficiency are described in detail (Sects. 2.2, 2.4). Then the three approaches are applied in different test cases of varying complexity, ranging from the NASA hump flow (Sect. 3.1), over the NACA0021 airfoil at stall (Sect. 3.2) up to the industry-relevant 3D Common Research Model in high-lift configuration (CRM-HL), cf. Sect. 3.3. The assessment focuses on potential grid point savings, while aiming to preserve the simulation accuracy compared to respective reference simulations, as well as experimental data.

2 Numerical Method

The flow computations in this paper are performed using the unstructured compressible finite-volume solver DLR-TAU, cf. Schwamborn et al. (2008). It uses 2nd-order schemes in both space and time, along with preconditioning for low-Mach number flows, to numerically solve the flow equations on mixed-element grids (containing e.g. tetrahedra, hexahedra, prisms).

In scale-resolving simulations a low-dissipation low-dispersion scheme (LD2) is employed, which combines an energy-preserving (skew-symmetric) convection flux operator of Kok (2009) with carefully-adjusted matrix-valued artificial dissipation as well as gradient-based flux reconstruction, cf. Löwe et al. (2016). To avoid numerical instabilities on unstructured grids for complex geometries, the scheme is typically applied in a hybrid form (HLD2). In this approach, a numerical sensor function for resolved turbulent flow regions, cf. Travin et al. (2002), is used to switch between the LD2 parameters in resolved-turbulence (i.e., LES) regions and a less accurate, but more robust standard scheme in unresolved flow regions, cf. Probst et al. (2016).

Time discretization of unsteady flows employs the implicit BDF2 scheme along with dual-time stepping, using an Backward-Euler method with LU-SGS solver for the inner (pseudo-time) iterations, cf. Langer et al. (2014).

2.1 Basic Hybrid RANS–LES Model

The present work considers both Delayed Detached-Eddy Simulation (DDES, Spalart et al. 2006) and Improved DDES (IDDES, Shur et al. 2008), which are specific extensions of the original Detached-Eddy Simulation (DES) for hybrid RANS–LES modelling. Building on the general DES concept, which involves inserting a hybrid length scale into an existing RANS turbulence model to transform it locally into a Smagorinsky-type LES sub-grid model, the DDES adds a boundary-layer sensor function to that length scale in order to shield attached flow against premature switching to LES mode, cf. Spalart et al. (2006). With these properties, DDES is well suited to simulate cases with rather clear distinction of attached and (strongly) separated flow, such as the NACA0021 at stall conditions, cf. Sect. 3.2.

For flows in which resolution of turbulence becomes relevant also in attached flow, the IDDES offers additional wall-modelled LES (WMLES) capabilities compared to DDES by further extending the hybrid length scale as:

$$l_{hyb} = \tilde{f}_d(1 + f_e)l_{RANS} + (1 - \tilde{f}_d)l_{LES} \tag{1}$$

In this blending of the original RANS-model scale, l_{RANS}, and the LES scale, $l_{LES} = C_{DES} \cdot \Delta$, the function $\tilde{f}_d = \max\left\{(1 - f_{dt}), f_B\right\}$ controls the switching between three different modelling modes, namely RANS, DES/LES and WMLES. In there, f_{dt} is the turbulent part of the RANS shielding function known from DDES, thus determining the overall switch between RANS and (WM)LES. The function f_B blends between RANS mode in the inner turbulent boundary and LES mode in the outer layer, thus controlling the WMLES branch of IDDES. It only depends on the grid spacings Δx_i and the wall distance d_w, reading:

$$f_B = \min\{2\exp(-9\alpha^2), 1.0\}, \tag{2}$$

where $\alpha = 0.25 - d_w/h_{max}$, $h_{max} = \max\{\Delta x_i\}$. Thanks to an extended formulation of the LES filter width Δ:

$$\Delta = \Delta_{\text{IDDES}} = \min\left\{\max\left[C_w \cdot d_w, C_w \cdot h_{\max}, h_{wn}\right], h_{\max}\right\}, \tag{3}$$

IDDES is able to apply one unique (but RANS-model-dependent) calibration coefficient in the LES length scale for different kinds of turbulent flow, such as wall-bounded or decaying isotropic turbulence. In Eq. (3), h_{wn} is the local wall-normal grid spacing and $C_w = 0.15$. For further details, refer to Shur et al. (2008).

2.2 Wall-Functions for Hybrid RANS–LES

While the near-wall RANS layers in DES-type models already serve as a form of wall-modelling (esp. in IDDES), they are classically resolved down to the wall with $y^+(1) \approx 1$ (Low-Re grid). Thus, wall functions may allow for additional grid coarsening in wall-normal direction. In the present work, we combine the wall functions of Knopp

(2006), Knopp et al. (2006) that were originally derived for RANS models, assuming that the near-wall RANS nature of DES justifies this approach. These wall functions are based on a carefully-adjusted blending of well-known wall laws, namely Spalding's (F_{Sp}), Reichardt's (F_{Rei}) and the logarithmic law of the wall (F_{Log}):

$$F_{\mathrm{Sp}}^{-1} = u^+ + 8.43\left(e^{0.41u^+} - \sum_{n=0}^{5} \frac{(0.41u^+)^n}{n!} \right), \quad F_{\mathrm{Log}} = \frac{\ln(y^+)}{0.41} + 5.1 \tag{4}$$

$$F_{\mathrm{Rei}} = \frac{\ln(1 + 0.4y^+)}{0.41} + 7.8\left(1 - e^{-\frac{y^+}{11}} - \frac{y^+}{11} e^{-\frac{y^+}{3}} \right) \tag{5}$$

By further calibrating the blending to match the low-Re solution of the RANS model they are used with, these wall functions are both RANS-model consistent and universal, meaning they are valid for a wide range of $y^+(1)$ under the assumption of zero pressure gradient.

The application with hybrid RANS–LES works in the same manner as for RANS, i.e. the friction velocity is computed from the wall function via Newton's method and the related wall shear stress is imposed at the wall. For increased efficiency in unsteady simulations, this evaluation can be performed only few times per physical time step without impairing the results. Verification and validation studies of this method for fundamental flows including separation (e.g. backward-facing step) have been presented in Herr and Probst (2021), showing decent agreement with low-Re solutions up to $y^+(1) \approx 25$.

2.2.1 Wall-normal grid adaptation for $y^+(1)$

Especially for complex 3D applications such as full aircraft (cf. Sect. 3.3), maintaining the mentioned acceptable $y^+(1)$ ranges is a major challenge, since strong local variations of the skin friction (and thus $y^+(1)$) are not known in advance and therefore cannot be taken into account in the initial mesh generation. As a remedy, we use a flow-solution-based adaptation of the near-wall grid resolution, which is controlled by a global target value, $y^+(1)_{target}$.

The method, which is described in detail in Knopp et al. (2006), computes the actual local $y^+(1)$ values in each surface node from an existing (preferably steady-RANS) flow solution and changes the first near-point distance $y(1)$ according to:

$$\begin{aligned} \text{if } \; y^+(1) > y^+(1)_{target} \; \text{ then set: } y(1)_{new} &= y(1) \cdot y^+(1)_{target} / y^+(1) \; ; \\ \text{else: } y(1)_{new} &= y(1) \; . \end{aligned}$$

To form a smooth and valid grid also away from the wall, the new distribution of point distances, $y(1)_{new}$, undergoes Laplacian smoothing on the surface, and the point distributions along the wall-normal rays above the surface (identified beforehand) are linearly altered up to a certain wall distance.

Since the wall-normal adaptation is implemented in an external tool outside of the flow solver, the computation of the current $y^+(1)$ values on high-Reynolds grids requires evaluation of wall functions within that tool, as well. Compared to the complex, RANS-model-dependent approach described in Sect. 2.2, a somewhat simplified wall function is used in the adaptation which is, however, considered sufficiently accurate for the given purpose.

2.3 Embedded Wall-Modelled LES

Embedded Wall-Modelled LES (EWMLES) is considered a means to restrict highly-resolved WMLES modelling to the critical flow regions of interest (e.g. local separation or shock-BL interaction), while imposing much cheaper RANS modelling in other areas. In the present paper we consider an EWMLES method based on the IDDES with some zonal treatment to provide both RANS and (WM)LES capabilities, which is combined with synthetic turbulence at the RANS–WMLES interface. The synthetic fluctuations are computed by the NTS-STG of Shur et al. (2014) and injected via local volume source terms in the momentum and energy equations. The functionality has first been implemented and validated using the DLR-TAU code for essentially 2D geometries (e.g. airfoils), see Francois et al. (2015), Probst and Ströer (2020) for details.

2.3.1 Improved Synthetic-Turbulence Forcing

In previous applications of the EWMLES approach, cf. Probst and Ströer (2020), Herr et al. (2023), the forcing of synthetic turbulence has been applied through the whole boundary layer down to the wall. Since the NTS-STG aims at reproducing the full Reynolds-stress profile that is provided as input (target) statistics, this leads to a potential doubling of the total (i.e., the sum of modelled and resolved) turbulent stress in the near-wall RANS layer of the WMLES mode of IDDES. This is confirmed by Fig. 1 (left), showing the relevant total shear stress in the STG-forcing region of a flat-plate flow with $Re_\Theta = 3040$ at the streamwise RANS–WMLES interface, which has been studied before e.g. in Deck et al. (2014), Probst and Ströer (2020).

One approach to resolve the strong near-wall overestimation of $\langle u'v' \rangle_{tot}$ is to reduce the input target stress for STG by the exact amount of existing modelled stress. While this correction has been successfully demonstrated in Probst and Ströer (2020) for the same test case, it also poses additional requirements, such as time averaging of velocity gradients and a sufficient streamwise extent of the forcing domain.

Therefore, a much simpler approach is considered here, where the forcing source term is constrained from being active in the near-wall RANS region. The RANS layer can be identified by the IDDES blending function f_B, which is used to modify the source term from Probst and Ströer (2020) as:

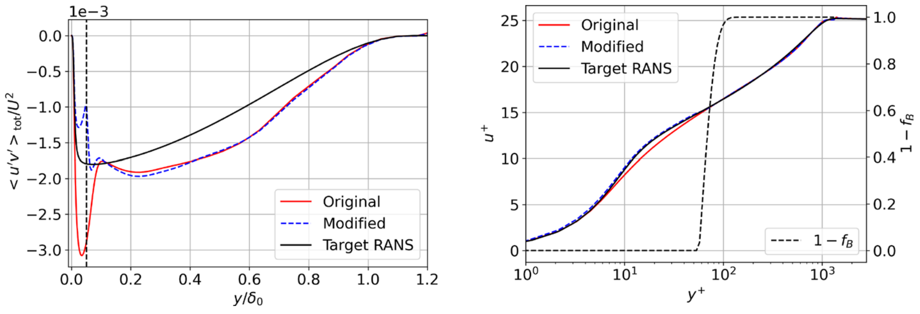

Fig. 1 Effect of different injection source terms on wall-normal profiles in the STG forcing region of a flat-plate flow. Left: Total (sum of modelled and resolved) turbulent shear stress. Right: Blending function $1 - f_B$ and resulting mean velocity profile

$$Q_i = (1 - f_B)\frac{\partial(\rho u_i')}{\partial t} \approx (1 - f_B)\frac{3(\rho u_i')^{n+1} - 4(\rho u_i')^{n} + (\rho u_i')^{n-1}}{2\Delta t} \tag{6}$$

with $u_i'^{n+1}$ being the target velocity fluctuation provided by the synthetic turbulence generator. As visible in Fig. 1 (left), this modified source term effectively reduces the stress peak close to the wall, even though now a moderate under-prediction can now be stated (due to an unexpected, slight positive resolved stress generated by the STG forcing). Note that the too large total stress around the centre of the boundary is caused by the modelled stress being convected from the upstream RANS region, calling for a more rapid reduction of turbulent viscosity to sub-grid level (not addressed here).

Figure 1 shows the velocity profile inside the forcing region, along with the distribution of the weighting factor $(1 - f_B)$. A discrepancy between the EWMLES and the RANS reference profile in the buffer layer, which is caused by the over-estimated total shear stress, is mitigated by using the modified source term. More importantly, also the pronounced peak in skin friction, c_f, at the RANS–LES interface is significantly decreased when using the modified source term, as shown in Fig. 2 (left). Moreover, the spurious noise peak is reduced to 25% of its original value at the interface, see the normalized root-mean-square value of the pressure fluctuations in Fig. 2 (right). All in all, this simple modification of the forcing term in the present EWMLES approach effectively improves some imperfections around the hybrid RANS–WMLES interface without complicating the implementation or impairing overall results.

2.3.2 Synthetic-Turbulence Injection on 3D Geometries

In a recent extension of the method to general 3D geometries, the dividing line between RANS and WMLES can now be defined by the user via polylines consisting of coordinates of multiple control points on the surface boundary. Surrounding the surface-projection of this polyline, the forcing volume for the synthetic-turbulence injection (typically half a boundary-layer thickness wide), as well as an upstream reference region for extracting RANS input data for the STG are placed automatically.

The approach is sketched for a simple curved surface using an arbitrary polyline in Fig. 3 (left). Technically, the forcing region downstream of the polyline (as well as the upstream RANS extraction region, not explicitly shown here) is first marked on the geometry surface

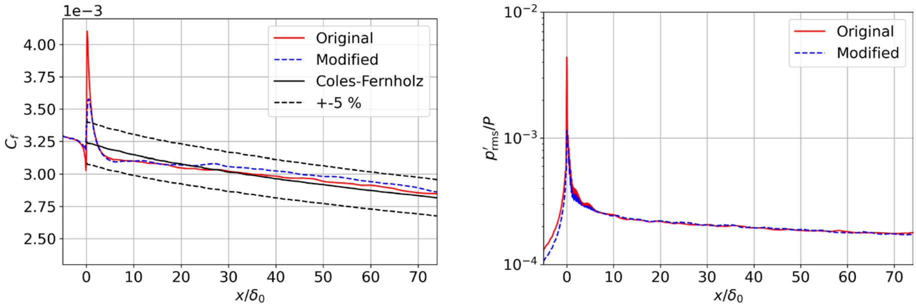

Fig. 2 Effect of different injection source terms on surface quantities along the flat-plate (with STG injection at $x/\delta_0 = 0$). Left: Mean skin friction distribution. Right: Root-mean-square of pressure fluctuations normalized by reference onflow pressure

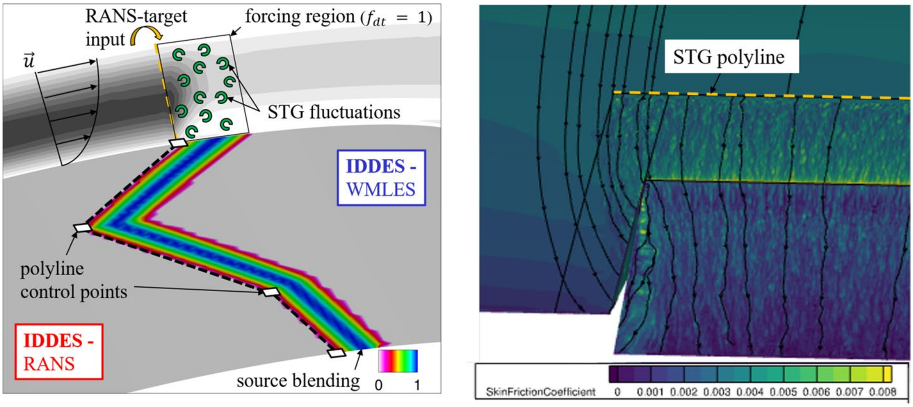

Fig. 3 Left: Principle sketch of present embedded WMLES method on 3D surfaces using synthetic turbulence injection along a user-defined polyline (the grey-shaded flow contour indicates the modelled-viscosity level). Right: Instantaneous skin friction and surface streamlines in an example application of the present EWMLES to a flow with strong lateral redirection, benefiting from the self-adapting RANS/WMLES modes downstream of the STG injection, provided by Streher (2024)

based on simple distance criteria. The surface marking is then communicated via an internal wall-normal data structure into the flow domain to mark the whole forcing volume. In wall-normal direction, the domain is bounded by the boundary-layer thickness, which is either approximately provided by the user or locally computed via some δ_{99}-criterion, cf. Probst et al. (2011). In flow direction, a simple Gaussian-distribution function $\in [0;1]$ is approximated within the forcing region which is multiplied with the volume source term (cf. Eq. 2.3.1) in order to smoothly blend the STG-injection for numerical robustness and reduced artificial noise.

Since the NTS-STG considers some non-local (or macro-scale) modelling parameters, cf. Shur et al. (2014), such as a bulk or reference velocity for computing the convection time scale, special care has to be taken, if these parameters vary strongly along the hybrid EWMLES interface. In that case, the current implementation allows separating the STG-injection front into multiple sections (defined by adjoining polylines), which may consider different values for the macro-scale parameters.

Compared to earlier EWMLES applications in Probst et al. (2017), Probst and Ströer (2020), where the upstream RANS and downstream WMLES modelling regions were defined by zonal markings (using geometric entities like boxes or cylinders), the approach has been further simplified by automatically enforcing the WMLES mode of IDDES by setting $f_{dt} = 1$ only within the forcing region derived from the polylines. As indicated in Fig. 3 (left), this local switch is sufficient to quickly reduce the eddy-viscosity from RANS to sub-grid level, while the intrinsic IDDES automatisms guarantee preservation of the WMLES mode also further downstream by means of convection (sufficient grid resolution provided). Note, that merely introducing synthetic turbulence without any (local) intervention in the hybrid modes of IDDES was found to delay transition to WMLES excessively.

In all other regions, the simulation may rely on the automatic (non-zonal) placement of RANS shielding and (WM)LES modelling by the IDDES functions, although an additional definition of RANS and WMLES zones is still possible for safety. Besides simplifying the setup of an EWMLES, this purely local enforcement of WMLES has the advantage, that the flow-parallel RANS–WMLES interface at the lateral boundary of the EWMLES domain may adapt naturally to redirections of the flow. This was found to be critical in an earlier EWMLES of an engine nacelle at incidence using fully pre-defined WMLES zones, where the lateral constriction of the flow generated a gap between the edge of the resolved-turbulence flow and the RANS region yielding reduced skin friction in that area, cf. Herr et al. (2023). An illustrative example, where the new approach circumvents this problem, is shown in Fig. 3 (right): for a STG-injection line placed upstream of a deflected control surface of a wing, the RANS–LES interface adapts even to strong inwards flow bending, yielding no sign of local skin-friction reduction at the edge of the resolved flow region.

2.4 Local Grid Adaptation in LES Regions

Since the spatial resolution for accurate LES of complex flow is difficult to determine a-priori, many grid designs exhibit high uniform resolution based on rather simple, partly global estimations. An adaptation of the grid resolution to the actual local requirements of LES may reduce the computational overhead, but implies suitable adaptation indicators as well as appropriate mesh refinement methods.

In the present work, the latter is provided by an external grid-adaptation module which subdivides the cell edges in unstructured grids based on given local solution-dependent refinement indicators and forms new valid cells with the help of transitional elements afterwards. It supports all cell types that can be handled by the flow solver, such as hexahedra, tetrahedra or pyramids, and causes little computational overhead compared to the overall simulation process, thanks to full MPI-based parallelization of both the adaption as well as the subsequent re-partitioning of the adapted grid, cf. Alrutz and Orlt (2006), Reuß et al. (2015).

Regarding local adaptations sensors suitable for LES, see Celik et al. (2009) for an overview, we consider on the one hand a criterion for “well-resolved LES” according to Pope (2004), demanding at least 80% of the total turbulent kinetic energy (TKE) to be resolved throughout the LES region:

$$TKE_{ratio} = \frac{k_{res}}{k_{total}} = \frac{k_{res}}{k_{res} + k_{sgs}} \geq 0.8 \tag{7}$$

While $k_{res} = \frac{1}{2}\left[\left(u_i - \langle u_i \rangle\right)^2\right]$ is obtained by statistical averaging of the flow over a sufficient time span, the modelled (sub-grid) energy k_{sgs} is approximated by explicit spatial top-hat filtering of the velocity field using a support size of 4, as suggested and explained in detail by Reuß et al. (2015).

As alternative indicator, we consider the SGS-viscosity-based variant of the index of resolution quality for LES of Celik et al. (2009) and also demand a value larger than 80%:

$$LES_{IQ} = 1 \Big/ \left[1 + \alpha_\nu \left(\frac{\langle \nu_{eff} \rangle}{\nu}\right)^n\right] \geq 0.8. \tag{8}$$

where $\alpha_\nu = 0.05$ and $n = 0.53$. The effective viscosity is assumed to be governed by the (sub-grid) eddy and molecular viscosities, $\nu_{eff} = \nu_t + \nu$, whereas contributions from numerical dissipation are neglected. This is justified by using the low-dissipation HLD2 scheme of Probst et al. (2016), briefly outlined in Sect. 2.

Following Reuß et al. (2015), after marking all those grid regions for refinement, where the criteria of either Eq. (7) or Eq. (8) are not fulfilled, we apply further conditions to allow refinement only in LES regions with resolved turbulent content. This is achieved by demanding the local resolved turbulence intensity, $Tu_{loc} = \sqrt{\frac{2}{3}k_{res}}/|u_i|$, to be larger than 0.1, as well as the hybrid model to operate in its LES mode, with $l_{hyb}/l_{RANS} < 1$. These "safeguard" criteria are particularly helpful in hybrid RANS–LES applications, since otherwise the above sensors would also mark large parts of the RANS (and non-turbulent onflow) regions for refinement.

The adaptation process starts from a statistically-converged hybrid RANS–LES solution obtained on a coarse grid, which is then iteratively refined based on either of the two indicators. Before the next adaptation step, another simulation run with sufficient transient and averaging time for the indicator evaluation is performed. In the present work, the averaging comprises several convective time units of the given flow problem for both indicators, neglecting potential optimizations of the process to reduce the sampling time. In that sense, the present investigation focuses on grid-point savings rather than overall process runtimes.

3 Test Cases and Results

In the following sections, we test and evaluate the methods for increasing the efficiency of hybrid RANS–LES simulations described in Sect. 2 on three different test cases with increasing complexity. While the combination with wall functions and the embedded WMLES method are applied up to an industrially relevant 3D test case, the investigations on LES adaptation are limited to 2D geometries. Where meaningful, quantitative statements on the computational effort are made in comparison to the basic hybrid method.

3.1 NASA Wall-Mounted Hump Flow

The hump flow of Greenblatt et al. (2006) is a common validation case for turbulence models and scale-resolving approaches. It is computed at $Re_c = 936,000$ (based on the hump length c) and $Ma = 0.1$. In all simulations, the lateral domain extends over 0.4 c, and SA-IDDES is used as hybrid RANS–LES model.

The grids used in both studies are unstructured, but dominated by hexahedra. The reference low-Reynolds grid, denoted below as *Fine (global)*, has around 2.8×10^6 grid points with 80 spanwise layers. It has been designed to provide a similar resolution with almost cubic cells ($\Delta x_i/c \approx 0.005$) in the LES regions as the structured grid used in Probst et al. (2017). Also other simulation parameters, such as temporal resolution ($\Delta = 0.002\ c/U_\infty$), the boundary-layer profile with $Re_\Theta = 7200$ prescribed at the inflow, as well as transient and statistical-averaging times are broadly in line with that study.

3.1.1 Wall Functions and Embedded WMLES

The first study focuses on the effect of wall functions, but also includes an EWMLES setup with synthetic turbulence injected just upstream of separation at $(x/c)_{STG} = 0.61$. The latter addresses a well-known challenge for (non-zonal) DDES or IDDES methods in the simulation of separating flows like the wall-mounted hump case, where the initial separated shear layer may exhibit delayed onset of resolved turbulence. As shown for example in Probst et al. (2017), this "grey area" at the RANS–LES interface can lead to a downstream shift of reattachment, but can be effectively mitigated by injecting synthetic turbulence upstream

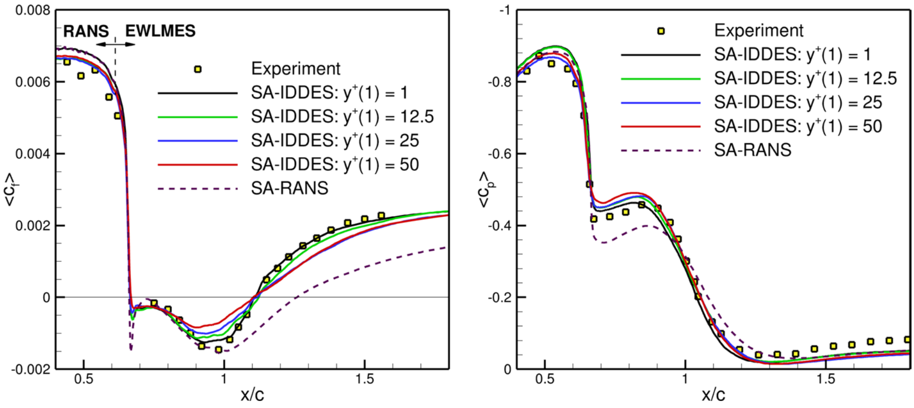

Fig. 4 Skin-friction (left) and surface pressure (right) on the NASA hump using EWMLES and wall functions on different grids

Table 1 Grid and simulation statistics using SA-IDDES with wall functions and EWMLES for the NASA hump flow

$y^+(1)$	1	12.5	25	50
Grid points, 10^6	3.53	2.54	2.34	2.16
Grid-point reduction vs. $y^+(1) = 1$, %	–	– 28.1	– 33.8	– 38.9
Error in separation length vs. exp., %	– 1.8	1.4	0.1	– 3.4
Run-time reduction vs. $y^+(1) = 1$, %	–	– 27.2	– 35.4	– 43.0

of the separation. In the present work, such a EWMLES setup is adopted in the study of wall functions, not only to avoid the grey-area effects but also to assess the feasibility of combining both approaches in a single simulation. As indicated by Fig. 4, the general embedded setup on the Low-Re grid, labelled as "SA-IDDES: $y^+(1) = 1$" (where $y^+(1)$ is measured on the hump crest), performs indeed well and yields close agreement with the measured skin friction. Also the surface pressure agrees overall well, but is overestimated after reattachment by all simulations, including RANS. This indicates a general uncertainty in the exact numerical representation of the experimental setup in this area, which, however, does not affect the present assessment of wall functions.

A variation of the first cell height while keeping the wall-normal growth rate constant yields three different grids with $y^+(1) = 12.5, 25, 50$. Computations on these grids using the present HRLM + WF approach retain the good predictions of the separation length up to the coarsest grid (cf. Table 1). However, in the recirculation and reattachment regions the deviations of the skin friction grow with increasing $y^+(1)$, in particular for values larger than 12.5. At the same time, the surface pressure in Fig. 4 (right) shows a less pronounced sensitivity to the $y^+(1)$ variation, especially in the reattachment region $x/c > 1.1$. Since the pressure evolution is closely linked with the displacement effect by the separation, this indicates that the shape and size of the separation bubble remain rather consistent despite the grid coarsening. The stronger variation in the skin friction, on the other hand, can be seen as a near-wall effect, which is more closely linked with the solution of the wall function itself. A more general formulation than Eqs. 4 and 5, which also takes into account the pressure gradient, could improve c_f beyond the already accurate prediction of the separation length.

As shown in Table 1, using the grid with $y^+(1) = 25$ can save more than a third of grid points and thus computing time, while the error in the predicted separation size remains minimal. Note that all simulations apply convergence criteria for the inner iterations of the implicit dual-time scheme, which explains some additional variations in the runtime speed ups.

3.1.2 LES Grid Adaptation

The second study on the hump flow considers the local indicator-based grid refinement in LES regions combined with pure SA-based IDDES without applying synthetic turbulence or wall functions. To this end, a coarse version of the Low-Re reference grid was created by reducing the resolution in the expected LES region by a factor of approximately 4 in each direction. This coarse version of the two fixed-grid levels (denoted as *Fine (global)* and *Coarse (global)*, respectively) serves as starting point for two independent adaptation runs using the indicators described in Sect. 2.4, which comprise up to 4 consecutive local refinement stages.

The resulting grids in the periodic lateral plane, as well as the achieved resolution of turbulent structures are visible in Fig. 5. The TKE_{ratio} indicator yields the strongest refinements in the initial separating shear layer and close to the near-wall RANS–LES interface, which can be seen in Fig. 5 (left) by the almost completely black areas in the lateral mesh plane. On the other hand, it yields only moderate (2×) and rather homogeneous refinement in the largest part of the separated flow. Note that the very near-wall region is marked for refinement, too, but omitted due to the adaptation restriction to LES regions, cf. Sect. 2.4.

The LES_{IQ} indicator yields a stronger refinement and, thus, finer resolved structures further downstream, whereas the initial shear layer and the near-wall regions are kept rather coarse. Accordingly, the (normalized) modelled turbulent viscosity ν_t/ν, which is displayed as colour-contour on the iso-surface of the Q-criterion in Fig. 5, yields larger values for the TKE_{ratio}- than for the LES_{IQ}-based adaptation in the separated region.

As for the resulting mean skin-friction distributions in Fig. 6, we first note that the Fine (global) grid returns the measured c_f-levels rather well. However, unlike the EWMLES in

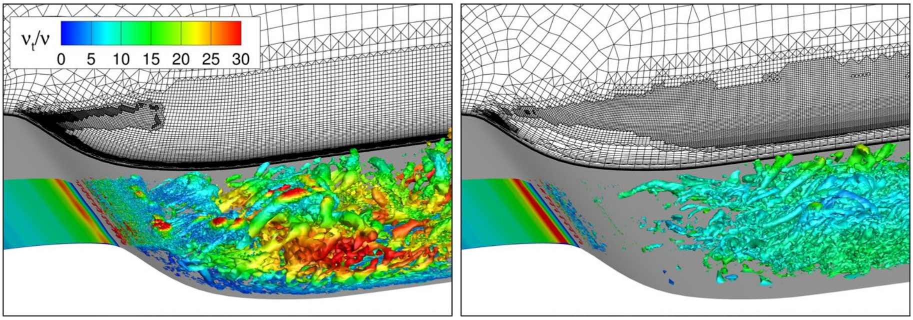

Fig. 5 Adapted NASA hump grids and iso-surfaces of Q-criterion (only shown in one half of the domain) coloured by the normalized turbulent viscosity after 4 consecutive refinement steps using TKE_{ratio} (left) and LES_{IQ} (right) as adaptation indicators

Table 2 Grids and results for the NASA hump flow using indicator-based grid adaptation in LES regions

Mesh/adaptation indicator	Grid points	Relative points versus fine (global), %	Separation-length Error versus exp., %
Coarse (global)	289,359	– 89.6	34.6
Fine (global)	2,796,525	–	10.8
TKE_{ratio} : 4×	3,382,107	– 20.9	5.2
TKE_{ratio} + near-wall: 2×	1,928,579	– 31.0	12.5
LES_{IQ} : 4×	2,340,729	– 16.3	16.4

Fig. 6 Skin-friction distribution on the NASA hump using SA-IDDES on global, as well as locally-adapted grid levels with number of refinement steps

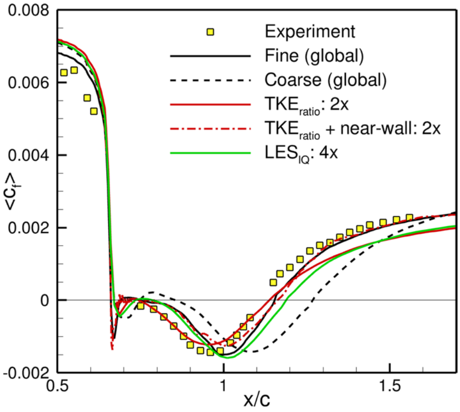

Sect. 3.1.1, the present simulation suffers from grey-area effects leading to a 10.6% delayed reattachment compared to the experiment, cf. Table 2. On the Coarse (global) grid, this delay is even increased to more than 34%.

Considering the adapted grids, the pronounced refinement of the initial shear-layer in the TKE_{ratio}-based refinement acts effectively on the grey-area issue and returns even closer agreement with the experiment in the separated region than the Fine (global) grid, e.g. regarding the location of minimum c_f. However, this comes at the cost of 21% more grid points compared to that reference mesh, as well as a delayed c_f-recovery after reattachment. Since the latter is also observed for the LES_{IQ} indicator, we attribute it to the chosen adaptation restrictions outlined in Sect. 2.4, which prevent refinement in all RANS areas including the near-wall layer of IDDES in WMLES mode.

To test this hypothesis, another adaptation run with the TKE_{ratio} indicator was performed, where the restrictions in the near-wall WMLES region were manually removed. Although this modified adaptation turned out to produce unsuitable meshes beyond the second refinement step because of highly-stretched transitional elements close to the wall, even that 2× adaption with 'TKE_{ratio} + near-wall' corrects the previous underestimation of the c_f recovery, as shown in Fig. 6. Moreover, the c_f prediction of that simulation agrees overall quite well with the results from the Fine (global) grid, while saving more than 30 % of grid points (cf. Table2).

Thus, the TKE_{ratio} indicator offers potential to not only recover the results on the reference grid at reduced cost, but also to alleviate local resolution deficits related to the grey area of hybrid RANS–LES. In contrast, with the LES_{IQ}-based adaptation a complete recovery, let alone improvement compared to the results on the Fine (global) grid is considered unlikely. This is because only little further refinement is requested after step 4, although with 16.4% error the computed separation length is still comparably far off from the experimental value (cf. Table2).

3.2 NACA0021 Airfoil at Stall

The NACA0021 airfoil at $\alpha = 60°$ ($Re = 2.7 \times 10^5$, Ma=0.15) is an aeronautical flow, which has become a popular test case for hybrid RANS–LES methods early on, cf. Travin et al. (2002), Weinman et al. (2006). Experimental data of the surface pressure are available from Swalwell et al. (2003). Due to the well-defined flow topology with massive separation in the airfoil wake, the SA-DDES is considered a suitable hybrid model for this case.

The basic simulation strategy follows the investigation by Weinman et al. (2006), using their fully-structured coarse (0.476×10^6 points) and fine (5.316×10^6 points) mesh levels as reference grids for a spanwise domain of 1 chord. Also, a uniform physical time step of $\Delta t = 2.5 \times 10^{-3} c_{ref}/U_\infty$ (with c_{ref} being the airfoil's chord length) is adopted on all grid levels which satisfies the convective CFL condition on the fine mesh.

Scale-resolving simulations of this flow are known to be sensitive not only to the grid resolution, but also to the spanwise domain width and the statistical sampling length, cf. Garbaruk et al. (2009) and Garbaruk et al. (2010). To obtain reference results, the simulations on the two global grids levels are computed over 400 convective time units (CTU $= c_{ref}/U_\infty$), where the last 300 are used to sample statistical averages. According to the "Concluding remarks" by Garbaruk et al. (2009), this sampling length fulfils just the bare minimum to obtain reliable statistics in this case, and even larger samples are recommended for the present domain width of one chord length. As these demands have been considered unfeasible for each iteration of the present grid-adaptation procedure, the following chapter includes an additional study to analyse the effect of longer sampling times on the statistically-averaged results.

3.2.1 LES Grid Adaptation

For the NACA0021 airfoil the local grid adaptation is assessed in a similar manner as for the hump flow, but this time applying up to 5 local refinement steps. The two structured grids with fixed (global) resolution levels from Weinman et al. (2006) (cf. Table 3) serve as reference, and the Coarse (global) is used as starting point for the adaptation runs. Both adaptation indicators, TKE_{ratio} and LES_{IQ}, are used as described in Sect. 2.4, while no additional near-wall refinement as in the hump flow needs to be considered.

A sampling interval of 100 CTU before each adaptation step ensures sufficient local statistical convergence of the refinement indicators, while it is rather short for obtaining reliable global statistics due to the dynamics of this particular flow (see the discussion in Sect. 3.2). Note, however, that the successive restarts from previous hybrid RANS–LES solutions in each adaptation step avoid the significant transient phase that occurs in common restarts from RANS or even free-stream solutions.

Regarding the outcome of the adaptation study, first consider the resulting grids in a 2D plane after 5 refinement steps using the TKE_{ratio} and LES_{IQ} indicators, respectively (cf. Fig. 7). In line with the behaviour in the hump flow, the TKE_{ratio} sensor focuses the refinement on the initial shear layers detaching from the airfoil's leading and trailing edges, but,

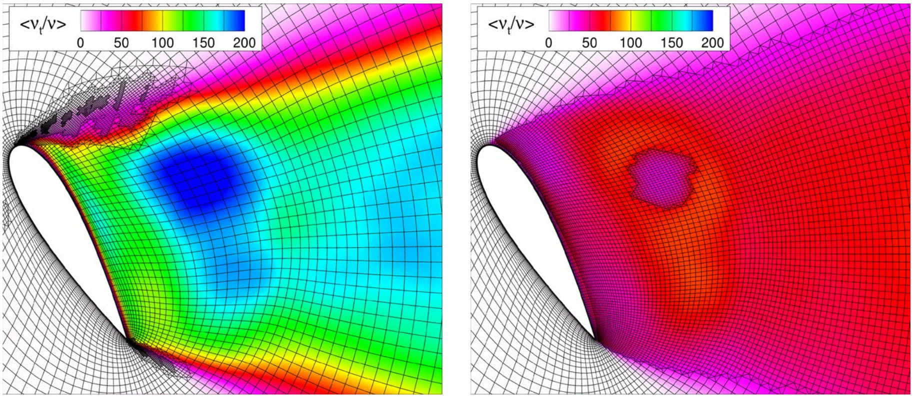

Fig. 7 Adapted NACA0012 grids after 5 refinement steps using TKE_{ratio}-based (left) and LES_{IQ}-based (right) adaptation, coloured by the normalized turbulent viscosity

surprisingly, fully retains the coarse resolution in most of the wake region (except for some local refinement far downstream). Consequently, significant grid-point savings of > 50 % are achieved compared to the Fine (global) grid, cf. Table 3. Note that already after 3× refinement based on TKE_{ratio}, the shear layers are resolved finer than by the Fine (global) grid.

In contrast, the LES_{IQ} indicator ignores again the initial shear layers and (moderately) refines the recirculation region, leading to different resolution and sub-grid-viscosity levels in the separated wake. Moreover, as even the wake far downstream (not visible in Fig. 7) is refined multiple times, a comparably huge grid size with more than 12 million points results from LES_{IQ}-based adaptation.

To assess the grid effects on the results, consider the time- and spanwise-averaged pressure distributions in Fig. 8 (left) in comparison with experimental data of Swalwell et al. (2003). First of all, the Coarse (global) grid yields the largest (negative) c_p levels on the suction side and, thus, the largest deviation from the experiment, while

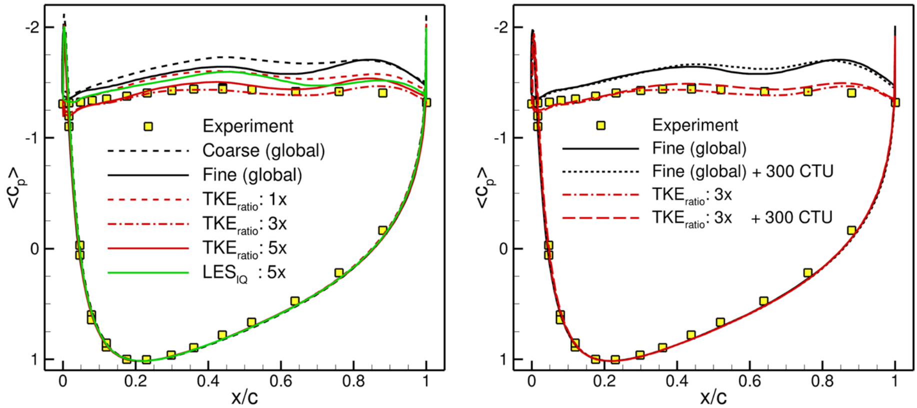

Fig. 8 Pressure distribution on NACA0012 using SA-DDES on global and locally-adapted grid levels. Left: Assessment of refinement indicators. Right: Effect of longer sampling time for selected grids

Table 3 Adaptation results for the NACA0012 case

Grid	Mesh points	Relative points versus fine (global), %
Coarse (global)	476,784	− 91.0
Fine (global)	5,316,444	–
TKE_{ratio} : 1×	551,575	− 89.6
TKE_{ratio} : 3×	1,510,993	− 71.6
TKE_{ratio} : 5×	2,501,627	− 52.9
LES_{IQ} : 5×	12,387,615	+ 133.0

all (global or local) grid refinements tend to decrease this deviation. Remarkably, the adaptation based on the TKE_{ratio} indicator yields clearly the largest effect on the results, closing the gap to the measured pressure plateau on the upper surface almost completely after only 3 refinement cycles. Moreover, this comes at only 30 % of the grid points of the Fine (global) reference mesh, which yields only slight improvement in the pressure prediction compared to the coarse initial mesh.

Note that already the first TKE_{ratio} adaptation step has a similar effect on c_p as the global refinement [i.e., Fine (global)], and also as the 5× adaptation based on LES_{IQ}, indicating a high relevance of the resolution of the shear layers at the airfoil's edges for accurate predictions of near-field flow. However, the uncertainties related to the numerical setup mentioned above, as well as the slightly larger deviations obtained after 5 adaptation cycles using TKE_{ratio} should motivate further investigations to verify these promising findings.

To this end, the effect of limited time sampling has been investigated by continuing the two most relevant simulations, namely on the Fine (global) and on the 3×-adapted grid using TKE_{ratio}, for an additional statistical averaging period of 300 CTU. According to Fig. 8 (right), the updated results show indeed a variation to the previous ones (amounting to 0.4 % and 2.4 % deviation in lift, respectively), but the important trends including the improved agreement of the adapted-grid result with the experimental data are robust. This indicates sufficient statistical confidence for the present evaluation of the LES-indicator-based grid adaptation, even though a detailed model validation as pursued e.g. in Garbaruk et al. (2009) may require further effort.

3.3 High-Lift Common Research Model

In order to evaluate two of the discussed approaches for increasing the efficiency of hybrid simulations on an industry-relevant configuration, we consider the flow around the Common Research Model in high-lift configuration (CRM-HL) at $Re = 5.45 \times 10^6$ and $Ma = 0.2$ and free-flight conditions as defined in the 4th High-Lift Prediction Workshop (Case 2a), cf. Ashton et al. (2022). On the one hand, DDES is combined with wall functions (cf. Sect. 2.2) to compute the relevant parts of the lift polar up to and beyond maximum lift. On the other hand, EWMLES simulations at two pre-stall angles of attack are conducted to demonstrate the general feasibility of the approach for a complex aeronautical flow, making use of the recent extensions presented in Sect. 2.3.

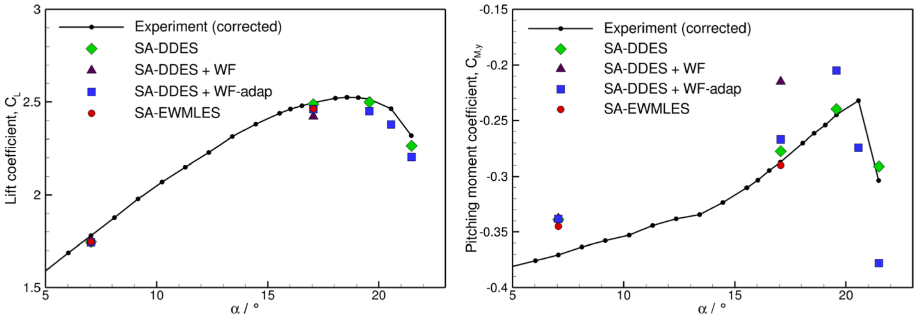

Fig. 9 Lift and pitching moment coefficients of the CRM-HL with reference data from experiments (Evans et al. 2020) and simulations (SA-DDES, Probst and Melber-Wilkending 2022b)

Fig. 10 Distribution of $y^+(1)$ in log-scale in the CRM-HL wing section 'Row H' at $\alpha = 17.05°$ for different grids

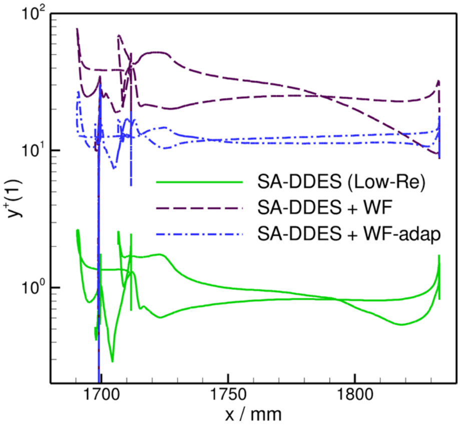

3.3.1 Wall Functions

The investigation of hybrid RANS–LES with wall functions applied to the CRM-HL builds upon SA-DDES simulations conducted on a Low-Reynolds workshop mesh with 218×10^6 points, which was generated with the meshing software ANSA from BETA CAE Systems. This unstructured mesh exhibits mostly hexahedral cells, both in the fine near-wall region and in the quickly-coarsening off-wall region up to the farfield boundary. The near-wall grid to discretize the boundary layer comprises 74 extruded grid layers and a first cell spacing above the wall that is fine enough to ensure $y^+(1) \approx 1-2$ (cf. Fig. 10). Additional local refinements are present in the expected separation and recirculation areas, in the vortex cores emerging from the wing and flap tips, as well as around the engine-nacelle strake. As presented in detail in Probst and Melber-Wilkending (2022b) and reproduced in Fig. 9, TAU simulations using SA-DDES and the HLD2 scheme show good agreement with measured lift and pitching moment coefficients especially at high angles of attack.

In the first step of the present investigation, starting with the ANSA input files for the Low-Re mesh, the wall-normal resolution close to the walls was reduced to meet an approximate (mean) $y^+(1)$ value of about 25, as suggested by previous studies (cf. Herr and Probst (2021) or Sect. 3.1). This new high-Reynolds mesh for wall functions (WF) yields about 125×10^6 grid points, yielding a reduction of −42.5 % compared to the Low-Re mesh, without impairing the resolution in the (partly separated) off-wall flow regions.

Apart from using the wall functions described in Sect. 2.2, the simulations on this grid (denoted as 'SA-DDES + WF') applied the same spatial and temporal as the reference 'SA-DDES' simulations from Probst and Melber-Wilkending (2022b): the hybrid low-dissipation low-dispersion (HLD2) scheme for the convective fluxes, a 2nd-order BDF2 time scheme with $\Delta t = 4 \times 10^{-4} c_{ref}/U_\infty$ (c_{ref}: mean aerodynamic chord) and a transient simulation time of at least 10 CTU after starting from a SA-RANS result, followed by at least 12 more CTU for statistical averaging (with larger intervals for higher angles of attack).

However, while the simulation at the lowest angle of attack, $\alpha = 7.05°$, agrees well with the Low-Re reference, the situation changes at $\alpha = 17.05°$, where the expected "staggered" separation pattern in the outer-wing region is replaced by one larger separation behind one of the slat brackets, cf. Fig. 11 (b) compared to (a), as well as the oil-flow picture from the experiment at slightly higher (but still comparable) angle of attack in Fig. 14 (right). This change in flow pattern is reflected in a significant offset in the pitching-moment coefficient along with a moderate lift drop compared to both the experimental and numerical (Low-Re) data, cf. Fig. 9.

Eventually, this behaviour was attributed to excessive values of $y^+(1) > 60$ that occur locally in the leading edge areas of both the slat and the wing as a result of increasing flow acceleration, cf. Fig. 10. With the help of the automatic y^+-adaptation method described in Sect. 2.2, several grids with different target (i.e., maximum) $y^+(1)$ values were generated and tested at $\alpha = 17.05°$. Recall that the y^+-adaptation only changes the (local) point distribution in wall-normal rays above the wall, while keeping the overall number of grid points in the mesh unchanged (125×10^6).

Remarkably, only a rather strong limitation to $y^+(1) = 12.5$ was found suitable to recover mostly acceptable agreement between the adapted-grid simulations (denoted as 'SA-DDES + WF-adap') and the low-Re reference result in terms of the integral coefficients (cf. Fig. 9), as well as (even though to a lesser extent) regarding the staggered outboard separation pattern, cf. Fig. 11. It should be noted, though, that the y^+-adaptation had to be performed at a rather low angle of attack of $\alpha = 7.05°$ in order to provide sufficiently

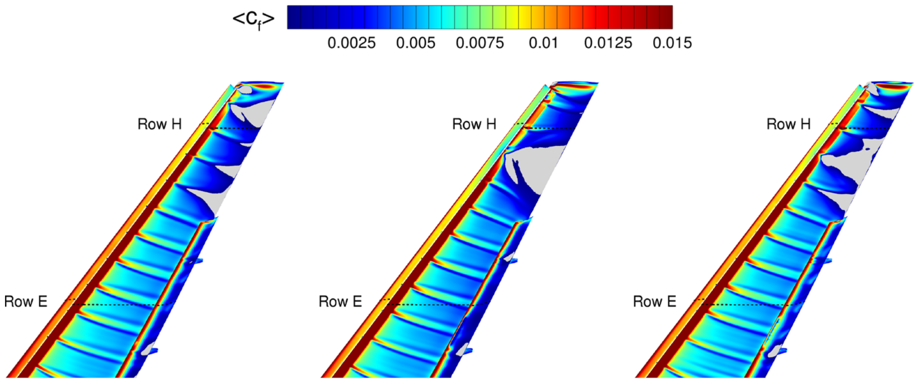

(a) SA-DDES (Low-Re) (b) SA-DDES + WF (c) SA-DDES + WF-adap

Fig. 11 Computed mean skin friction on the outboard CRM-HL wing at $\alpha = 17.05°$ (light-grey colour indicates backflow) smooth, steady surface flow data as input for the adaptation method. Because of this, the resulting $y^+(1)$ values at higher angles may locally exceed the target value of 12.5, as visible for $\alpha = 17.05°$ in Fig. 10.

The pressure distributions at $\alpha = 17.05°$ shown in Fig. 12 (left) for different spanwise cut-sections along the wing (Row A: close to the wing root, Row E and H: see Fig. 11) confirm a significant loss of local lift with the non-adapted grid ('SA-DDES + WF') in the outboard wing section H, which is largely remedied by the y^+-adaptation. Even more, the 'SA-DDES + WF-adap' agrees best with the experiment in this section, whereas as the Low-Re simulation exhibits excessive separation beyond Row H (visible in Fig. 11), affecting the pressure recovery in that area. However, judging from the flow pattern, a similar issue may exist for the 'SA-DDES + WF-adap' a bit more inboard, too. Apart from that, Fig. 12 reveals overall good agreement between the simulations with wall functions and the low-Re reference simulation, not only in terms of surface pressure (left), but also concerning the more challenging prediction of the (streamwise) skin friction $c_{f,x}$ (right).

For further 'SA-DDES + WF-adap' simulations at higher angles of attack around and beyond maximum lift, only the integral lift and moment coefficients in Fig. 9 are discussed. While the quantitative agreement decreases, especially for the moment coefficient, the general trends of lift collapse and pitch break, as well as the angle of maximum lift are still in line with the experimental and numerical references. Note that the moment coefficient of the CRM-HL configuration was found sensitive to subtle changes in the separation patterns and, therefore, is hard to predict not only for RANS, but also for scale-resolving simulation approaches, cf. Ashton et al. (2022), Probst and Melber-Wilkending (2022b). Also recall the increasing offset to the flow conditions, that serve as input for the y^+-adaptation ($\alpha = 7.05°$), giving further explanation for the deviations at higher α and a starting point potential improvement. With these considerations in mind, we conclude an overall acceptable applicability of the wall-function-based hybrid approach for simulating complex aeronautical flow.

Regarding the efficiency gain resulting from the use of wall functions instead of the fully resolved Low-Re mesh, the relative reduction in the number of grid points (−42.5 %) translates roughly into a corresponding runtime speed up, which amounts to about − 40 % in the average wall-clock time per solver iteration. Thus, even for a complex 3D geometry, the additional effort required to solve the (partially implicit) wall functions is almost negligible, mainly due to the reduced evaluation frequency applied in implicit unsteady simulations, cf. Sect. 2.2.

An additional influence on the overall runtime may be expected due to the improved numerical stiffness properties of wall-function meshes, which result from the reduced aspect ratios of the near-wall cells (cf. Sect. 3.1.1). However, this effect is difficult to quantify and generalize based on such a complex flow case, as it may depend on specific solver methods or settings, and could be superimposed by unrelated (local) convergence issues. Therefore, it is not part of the present investigation.

3.3.2 Initial Assessment of Embedded WMLES

Complementary to the use of wall functions, we investigate the feasibility and efficiency potential of applying the embedded wall-modelled LES approach from Sect. 2.3 to the industry-relevant CRM-HL case. While there is no expectation to reduce the computational cost compared to e.g. DDES with wall functions, the idea is to apply highly-resolved local WMLES only in critical flow regions and to consider a corresponding global WMLES

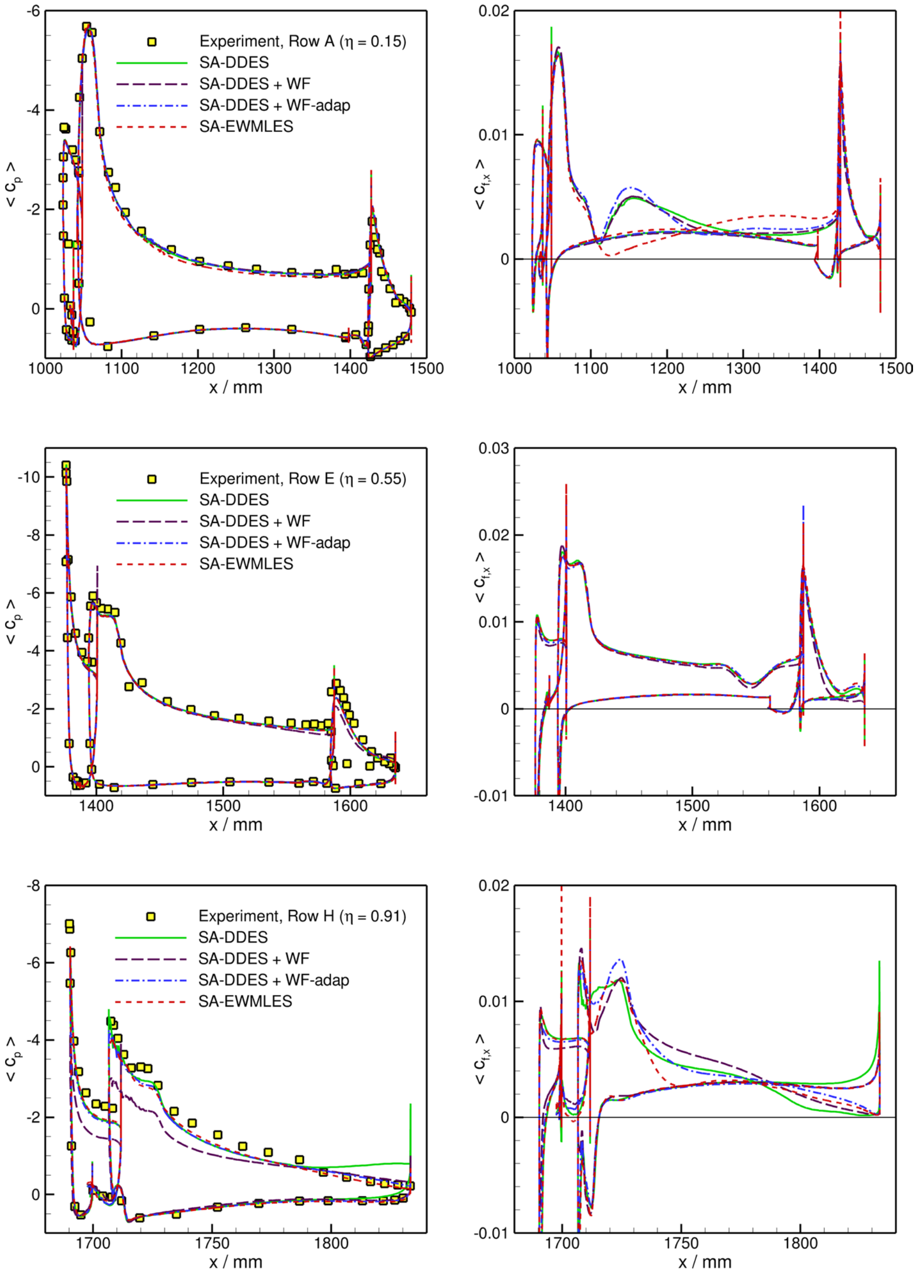

Fig. 12 Pressure (left) and skin-friction (right) distributions in different wing sections of the CRM-HL at $\alpha = 17.05°$, where η is the spanwise location on the stowed configuration normalized by the wing semi-span

(e.g., an IDDES of the whole high-lift wing of an aircraft, cf. Probst and Melber-Wilkending (2022a) as reference. Thus, the goal is to assess the potential for even higher accuracy than a global DDES (or under-resolved WMLES) at acceptable computational effort.

For an initial assessment, we chose the outboard upper wing area, where first considerable separations may strongly affect the aerodynamics (cf. Ashton et al. 2022; Probst and Melber-Wilkending 2022b, as well as the previous section), as the only EWMLES region in this study (even though the present EWMLES approach allows multiple separate synthetic-turbulence injections).

To this end, the outer 25% of the upper-side wing of the low-Re grid (218×10^6 points) were isotropically refined by a factor of 4 in each wall-tangential direction, see Fig. 13 (left). While the original wall-normal resolution with an initial growth rate of ≤ 1.1 is considered suitable for IDDES in WMLES mode, the wall-tangential refinement ensures for the normalized spacing in wall units, $\Delta x^+_{tan} < 400$, as well as $\Delta x_{tan}/\delta \approx 0.1 - 0.2$ over the largest part of the outer wing section (δ being the local boundary layer thickness).

With a resulting grid size of 282×10^6 points, the local refinement of about 20% of the upper wing surface yields an overall point increase of less than 30%. Linear extrapolation of this point increase to the whole (upper and lower) wing surface would yield around 860×10^6 points for a theoretical global WMLES (using IDDES). A similar number, namely 780×10^6 points results if the global IDDES grid for the JAXA standard model used in Probst and Melber-Wilkending (2022a) is extrapolated linearly in terms of the respective Reynolds numbers, as suggested by Choi and Moin (2011) for estimating WMLES grid-point requirements. Note that additional savings for the EWMLES mesh could be achieved by reducing the resolution in the surrounding RANS regions relative to the DDES resolution of the original grid, and potentially by combining the approach with wall functions as demonstrated in Sect. 3.1.

EWMLES simulations on this mesh have been conducted at two pre-stall angles of attack with only up to moderate outboard separation, $\alpha = 7.05°$ and $17.05°$, allowing to place the hybrid RANS–WMLES interface with one common polyline setup for both angles. Compared to the SA-DDES simulations in the previous paragraph, the temporal resolution had to be increased by a factor of two, yielding $\Delta t = 2 \times 10^{-4} c_{ref}/U_\infty$, in order to ensure a convective CFL number ≤ 1 in the WMLES area.

As depicted in Fig. 13, the hybrid interface (red line) is placed via one straight polyline that follows the sweep angle at around 15 % of chord of the main-wing

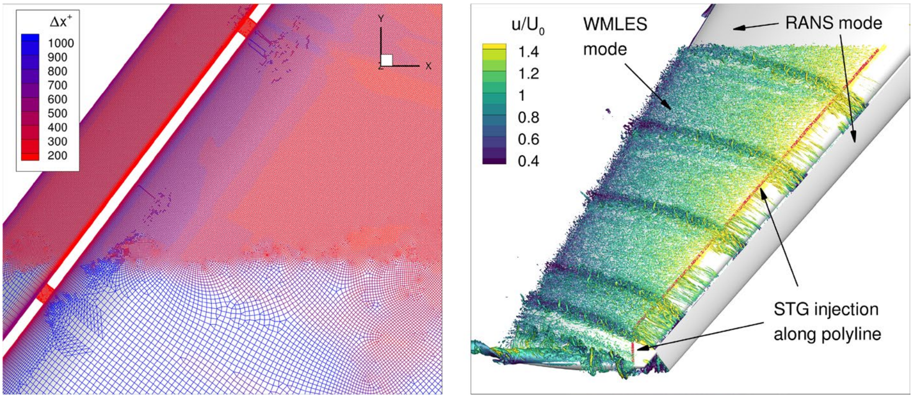

Fig. 13 Left: Outboard surface-mesh refinement for EWMLES of the CRM-HL, coloured by normalized streamwise grid spacing in wall units. Right: Iso-surface of Q-criterion, $Q_{iso} = 2000\ U_0^2/c_{ref}^2$, in the EWMLES of the CRM-HL at $\alpha = 7.05°$, with synthetic-turbulence injection at polyline (red)

element, and a second, unswept polyline (with different local macro-scale parameters, cf. Sect. 2.3) for the wing-tip region. The iso-surface of the Q-criterion visualizes the injection and subsequent development of turbulence in the boundary layer flow along that interface, but also reveals interactions with incoming turbulent structures emerging from the slat tracks. The rather abrupt spanwise truncation of resolved turbulence towards the inner wing region is due to a manual enforcement of RANS mode in order to prevent the IDDES from switching to (WM)LES outside of the target EWMLES area.

With this setup, EWMLES simulations at both angles of attack were conducted up to statistical convergence. The integral coefficients in Fig. 9 show good agreement with the reference SA-DDES simulations in terms of lift (left), and even some improvement towards the experimental data in terms of the pitching moment (right). This finding it backed by satisfying predictions of the measured pressure distributions at $\alpha = 17.05°$, both in the RANS region (Rows A and E) as well as in the EWMLES area (Row H), cf. Fig. 12 (left). Regarding the skin friction in Fig. 12 (right), however, larger deviations from the other numerical simulations are observed. In Row A, the RANS modelling of the vortex emerging from the inner slat-tip may cause a distinct difference compared to the well-resolved vortex in the SA-DDES simulations (cf. Probst and Melber-Wilkending (2022b). In the EWMLES region in row H, the somewhat stronger dip in $c_{f,x}$ around $x = 1750$ mm may indicate a delay of fully-developed turbulent flow after the hybrid interface, but there is no validation data to support this.

On the contrary, the comparison of separation patterns with the oil-flow picture at a slightly higher angle of attack in Fig. 14 yields reasonable qualitative agreement and a better representation of the staggered separation than obtained with DDES (cf. 11). Thus, although only set up as an initial demonstration and assessment of the present EWMLES approach for complex high-lift aircraft, the results support the hypothesis that such a local highly-resolved approach offers improved accuracy potential at affordable computational effort.

4 Conclusions

Three different approaches for reducing the computational effort of scale-resolving simulations with hybrid RANS–LES have been studied, namely:

Fig. 14 Left: Skin friction on the outboard CRM-HL wing at $\alpha = 17.05°$ computed with EWMLES (colour legend corresponds to Fig. 11, light-grey indicates backflow). Right: Oil-flow picture on the CRM-HL outer wing area from the wind-tunnel experiment at $\alpha = 17.98°$ (uncorrected), cf. Evans et al. (2020)

(a) The combination of wall functions with hybrid models such as DDES or IDDES, which allows a reduction of the wall-normal resolution near the surface by bridging the inner parts of boundary layer.
(b) Local mesh adaptation in the LES regions of hybrid RANS–LES, where two different refinement indicators are applied and compared with simulations on grids with (mostly) uniform LES resolution.
(c) An extended embedded wall-modelled LES approach based on hybrid RANS–LES and synthetic-turbulence injection, which has been generalized for complex 3D applications. This method allows to restrict the turbulence-resolving branch of the hybrid simulation to critical regions of the boundary layer flow, e.g. those subjected to strong pressure gradients and incipient separation. Compared to a global wall-modelled LES, considerably savings in grid points are possible.

The methods were implemented in an unstructured compressible finite-volume solver and assessed for different test cases, ranging from fundamental 2D flows up to an industry-relevant 3D aircraft geometry in high-lift configuration.

While wall functions and local grid adaptation yield rather obvious potential for grid-point savings relative to standard (rather homogeneous, low-Reynolds) hybrid RANS–LES grids, the embedded WMLES needs to be compared to a (hypothetical) global WMLES, e.g. using IDDES with corresponding grid resolution, in order to exhibit efficiency gains. With this in mind, the main findings of the study are:

- The combination of wall functions with either DDES or IDDES retains excellent agreement with the measured separation length in the NASA hump flow, but also acceptable predictions of the stall behaviour (e.g. angle of maximum lift, pitch break) in the complex CRM-HL flow, as long as the wall-normal spacing does not exceed $y^+(1) \leq 12.5 - 25$. Even with that limited coarsening compared to the respective low-Re grid, overall run-time savings of more than -35 % are achieved for both cases.
- A refinement indicator based on the ratio of resolved to total TKE appears suited for adapting the LES grid regions in hybrid RANS–LES, as demonstrated for the two fundamental, yet rather different flows over the NASA hump and the NACA0021 at $\alpha = 60°$. In both cases, the accuracy of the respective Fine (global) meshes could either be retained at significantly reduced grid sizes (− 31 % for the hump, -71 % for the NACA0021), or even improved at limited and partly no additional grid points. To achieve this, the ability of the TKE_{ratio}-based adaptation to reduce the grey areas in the initial shear layers by local refinement appears crucial.
- A modified synthetic-turbulence forcing for EWMLES, which takes the near-wall RANS layer of IDDES into account, was shown to reduce previous disturbances, e.g. in the velocity profile and the skin friction, at the RANS–WMLES interface.
- This EWMLES approach along with a recent extension for easy applicability to general 3D geometries was successfully demonstrated for the CRM-HL. The local WMLES of the critical outer-wing region was not only estimated to save at least -63 % of grid points relative to a global IDDES, but also showed the overall best agreement with experimental data at $\alpha = 17.05°$ among the considered simulation approaches, including integral lift and moment coefficients, pressure distributions on the wing, as well as separation patterns in the outboard wing area.

A combination of these methods should even offer accumulated effects, but this was only tackled through a successful demonstration of EWMLES along with wall functions for the NASA hump flow. Additional studies on the CRM-HL flow are needed to explore the feasibility and efficiency potential of the combined methods for industry-relevant cases. Further limitations of the present study include the unexpected large errors in the wall-function simulations of the CRM-HL even at moderate $y^+(1)$ values, which could be remedied only to a limited extent by strong wall-normal grid adaptation. While this finding supports the value of such a grid adaptation in combination with the use of wall functions, one topic for future research is the use of more elaborate wall functions in order to allow for stronger near-wall coarsening, e.g. by taking the local pressure gradient into account. The investigation of grid adaptation in LES regions has not yet gone beyond 2D geometries, while the iterative process lacks a stopping criterion to determine when the adaptation result is considered sufficient. Thus, apart from assessing its applicability to industry-relevant 3D cases, future studies need to consider the impact and possible optimizations of the iterative refinement process, which has to be taken into account for a fair assessment of its efficiency potential. At this point it should be noted that while the need for statistically well-converged solutions to evaluate the TKE_{ratio} indicator may seem overly demanding, the initial simulation stages on much coarser meshes than the respective Fine (global) grid are comparably inexpensive. Finally, while the EWMLES was successfully demonstrated for operating conditions close to maximum lift, an application beyond this point may uncover additional complexities due to the increasing unsteadiness of the separated flow regions.

Despite these limitations, the findings of this paper mark important steps towards more efficient hybrid RANS–LES, as all three approaches offer the potential for significant savings in grid points and runtime.

Acknowledgements The authors gratefully acknowledge the organizers and contributors of the 4th High-Lift Prediction Workshop for providing common grids and experimental data for the CRM-HL case. The authors are thankful to Dr. Stefan Melber-Wilkending (DLR Braunschweig) for providing modified meshes of the CRM-HL that are suitable for wall functions and embedded WMLES, respectively. The authors gratefully acknowledge the scientific support and HPC resources provided by the German Aerospace Center (DLR). The HPC system CARO is partially funded by "Ministry of Science and Culture of Lower Saxony" and "Federal Ministry for Economic Affairs and Climate Action".

Author Contributions A.P. conceptualized and conducted most parts of the research, and created the main part of the text and figures. E.S. conducted the research on the improved synthetic-turbulence forcing and provided the related text and figures. S.P. conducted software extensions for the LES grid-adaptation indicators and contributed to the related research. M.O. conducted general software extensions for the grid adaptation and contributed to the related research. T.K. provided software extensions for the wall-normal grid adaptation and wall functions and contributed to the related research. All authors reviewed the manuscript.

Funding Open Access funding enabled and organized by Projekt DEAL. The funding of this work by the DLR internal aeronautical program within the project ADaMant is gratefully acknowledged.

Data Availability The simulation data is stored on DLR premises and is not publicly accessible. Processed data could be made available upon request. This requires permission by DLR.

Declarations

Ethical Approval I confirm that the authors have upheld the integrity of the scientific record, thereby complying with the journal's ethics policy.

Conflict of interest I declare that the authors have no Conflict of interest as defined by Springer, or other interests that might be perceived to influence the results and/or discussion reported in this paper.

Informed Consent I confirm that all of the material is owned by the authors and/or no permissions from third parties are required.

References

Alrutz, T., Orlt, M.: Parallel dynamic grid refinement for industrial applications. In: Wesseling, P Oñate., Périaux, E., J, (eds.) Proceedings of c2006. The Netherlands, TU Delft (2006)

Ashton, N., Batten, P., Cary, A., et al.: HLPW-4 / GMGW-3 : Hybrid RANS/LES Technology Focus Group Workshop Summary. In: AIAA 2022-3293 (2022)

Benard, P.: Mesh adaptation for large-eddy simulations in complex geometries. Int. J. Numer. Methods Fluids **81**(2016), 719–740 (2016)

Celik, I., Klein, M., Janicka, J.: Assessment measures for engineering LES applications. J. Fluids Eng. Trans. ASME **131**(3), 0311021–03110210 (2009). https://doi.org/10.1115/1.3059703

Choi, H., Moin, P.: Grid-point requirements for large eddy simulation: Chapman's estimates revisited. Center Turbul. Res. Ann. Res. Briefs **2011**, 31–36 (2011)

Deck, S., Renard, N., Laraufie, R., et al.: Zonal detached eddy simulation (ZDES) of a spatially developing flat plate turbulent boundary layer over the Reynolds number range 3 150 <= ReΘ < = 14 000. Phys. Fluids (2014). https://doi.org/10.1063/1.4866180

Evans, A.N., Lacy, D.S., Smith, I., et al.: Test summary of the NASA high-lift common research model half-span at QinetiQ 5-Metre pressurized low-speed wind tunnel (2020). https://doi.org/10.2514/6.2020-2770, https://doi.org/10.2514/6.2020-2770

Francois, D.G., Radespiel, R., Probst, A.: Forced synthetic turbulence approach to stimulate resolved turbulence generation in embedded LES. Notes Numer. Fluid Mech. Multidiscip. Des. **130**, 81–92 (2015). https://doi.org/10.1007/978-3-319-15141-0_6

Garbaruk, A., Leicher, S., Mockett, C., et al.: Evaluation of time sample and span size effects in des of nominally 2D airfoils beyond stall. Notes Numer. Fluid Mech. Multidiscip. Des. **111**, 87–99 (2010). https://doi.org/10.1007/978-3-642-14168-3_7

Garbaruk, A.V., Shur, M.L., Strelets, M.K., et al.: NACA0021 at 60° Incidence. "DESider–a European effort on hybrid RANS-LES modelling''. Notes Numer. Fluid Mech. Multidiscip. Des. **103**, 127–139 (2009)

Greenblatt, D., Paschal, K.B., Yao, C.S., et al.: Experimental investigation of separation control part 1: baseline and steady suction. AIAA J. **44**(12), 2820–2830 (2006). https://doi.org/10.2514/1.13817

Herr, M., Probst, A.: Efficient modelling of near-wall turbulence in hybrid RANS–LES simulations. Notes Numer. Fluid Mech. Multidiscip. Des. **151**, 615–624 (2021). https://doi.org/10.1007/978-3-030-79561-0_58

Herr, M., Probst, A., Radespiel, R.: Grey area in Embedded WMLES on a transonic nacelle-aircraft configuration. CEAS Aeronaut. J. (2023).https://doi.org/10.1007/s13272-023-00664-z, arXiv:2301.05299

Jägerskupper, J., Vollmer, D.: On highly scalable 2-level-parallel unstructured Cfd. In: World Congress in Computational Mechanics and ECCOMAS Congress (June), pp. 1–12 (2022). https://doi.org/10.23967/eccomas.2022.208

Jarrin, N., Prosser, R., Uribe, J.C., et al.: Reconstruction of turbulent fluctuations for hybrid RANS/LES simulations using a synthetic-eddy method. Int. J. Heat Fluid Flow **30**(3), 435–442 (2009)

Knopp, T.: Model-consistent universal wall-functions for RANS turbulence modelling. In: Proceedings International Conference BAIL, pp. 1–8 (2006). http://www.num.math.uni-goettingen.de/bail/documents/proceedings/knopp.pdf

Knopp, T., Alrutz, T., Schwamborn, D.: A grid and flow adaptive wall-function method for RANS turbulence modelling. J. Comput. Phys. **220**(1), 19–40 (2006). https://doi.org/10.1016/j.jcp.2006.05.003

Kok, J.: A high-order low-dispersion symmetry-preserving finite-volume method for compressible flow on curvilinear grids. J. Comput Phys. **228**(18), 6811–6832 (2009)

Langer, S., Schwöppe, A., Kroll, N.: The DLR flow solver TAU—status and recent algorithmic developments. In: AIAA 2014-0080, 52nd Aerospace Sciences Meeting (2014). https://doi.org/10.2514/6.2014-0080

Limare, A., Borouchaki, H., Brenner, P.: Adaptive mesh refinement with an automatic hybrid RANS/LES strategy and overset grids. In: Hoarau, Y., Peng, S.H., Schwamborn, D., et al. (eds.) Progress in Hybrid RANS-LES Modelling, pp. 159–168. Springer, Cham (2020)

Löwe, J., Probst, A., Knopp, T., et al.: Low-dissipation low-dispersion second-order scheme for unstructured finite-volume flow solvers. AIAA J. **54**(10), 2961–2971 (2016)

Mockett, C., Fuchs, M., Thiele, F.: Progress in DES for wall-modelled LES of complex internal flows. Comput. Fluids **65**, 44–55 (2012). https://doi.org/10.1016/j.compfluid.2012.03.014

Pope, S.B.: Ten questions concerning the large-eddy simulation of turbulent flows. New J. Phys. **6**, 35–35 (2004). https://doi.org/10.1088/1367-2630/6/1/035

Probst, A., Melber-Wilkending, S.: Hybrid RANS/LES of a generic high-lift aircraft configuration near maximum lift. Int. J. Numer. Methods Heat Fluid Flow **32**(4), 1204–1221 (2022). https://doi.org/10.1108/hff-08-2021-0525

Probst, A., Melber-Wilkending, S.: Numerical and modeling investigations of the high-lift CRM configuration using hybrid RANS/LES. In: AIAA, pp. 2022–3590 (2022b). https://doi.org/10.2514/6.2022-3590

Probst, A., Ströer, P.: Comparative assessment of synthetic turbulence methods in an unstructured compressible flow solver. Notes Numer. Fluid Mech. Multidiscip. Des. **143**, 193–202 (2020). https://doi.org/10.1007/978-3-030-27607-2_15

Probst, A., Radespiel, R., Knopp, T.: Detached-Eddy simulation of aerodynamic flows using a reynolds-stress background model and algebraic RANS/LES sensors. In: AIAA Paper 2011-3206 (2011)

Probst, A., Löwe, J., Reuß, S., et al.: Scale-resolving simulations with a low-dissipation low-dispersion second-order scheme for unstructured flow solvers. AIAA J. **54**(10), 2972–2987 (2016)

Probst, A., Schwamborn, D., Garbaruk, A., et al.: Evaluation of grey area mitigation tools within zonal and non-zonal RANS-LES approaches in flows with pressure induced separation. Int. J. Heat Fluid Flow **68**, 237–247 (2017). https://doi.org/10.1016/j.ijheatfluidflow.2017.08.008

Probst, A., Knopp, T., Grabe, C., et al.: HPC requirements of high-fidelity flow simulations for aerodynamic applications. In: Euro-Par 2019: Parallel Processing Workshops Euro-Par 2019 Lecture Notes in Computer Science, vol. 11997, pp. 375–387 (2020). https://doi.org/10.1007/978-3-030-48340-1_29

Reuß, S., Knopp, T., Probst, A., et al.: Assessment of local LES-resolution sensors for hybrid RANS/LES simulations. In: Progress in Hybrid RANS-LES Modelling Notes on Numerical Fluid Mechanics and Multidisciplinary Design, vol. 130. Springer (2015)

Schwamborn, D., Gardner, A.D., von Geyr, H., et al.: Development of the DLR TAU-code for aerospace applications. In: International Conference on Aerospace Science and Technology 26–28 June 2008, Bangalore, India (2008)

Shur, M.L., Spalart, P.R., Strelets, M.K., et al.: A hybrid RANS–LES approach with delayed-DES and wall-modelled LES capabilities. Int. J. Heat Fluid Flow **29**(6), 406–417 (2008)

Shur, M.L., Spalart, P.R., Strelets, M.K., et al.: Synthetic turbulence generators for RANS–LES interfaces in zonal simulations of aerodynamic and aeroacoustic problems. Flow Turbul. Combust. **93**, 63–92 (2014). https://doi.org/10.1007/s10494-014-9534-8

Spalart, P.R., Deck, S., Shur, M.L., et al.: A new version of detached-eddy simulation, resistant to ambiguous grid densities. Theoret. Comput. Fluid Dyn. **20**(3), 181–195 (2006). https://doi.org/10.1007/s00162-006-0015-0

Stoellinger, M.K., Mokhtarpoor, R., Heinz, S.: Hybrid RANS–LES modeling using smooth and rough wall functions. In: AIAA 2019-1576, AIAA Scitech 2019 Forum (2019). https://doi.org/10.2514/6.2019-1576, https://doi.org/10.2514/6.2019-1576

Streher, L.B.: Personal communication (2024)

Swalwell, K.E., Sheridan, J., Melbourne, W.H.: Frequency analysis of surface pressures on an airfoil after stall. 21st AIAA Applied Aerodynamics Conference (June), pp. 1–8 (2003). https://doi.org/10.2514/6.2003-3416

Toosi, S., Larsson, J.: Towards systematic grid selection in LES: identifying the optimal spatial resolution by minimizing the solution sensitivity. Comput. Fluids **201**, 104488 (2020). https://doi.org/10.1016/j.compfluid.2020.104488

Travin, A., Shur, M., Strelets, M., et al.: Physical and numerical upgrades in the detached-eddy simulation of complex turbulent flows. Adv. LES Complex Flows **65**(5), 239–254 (2002)

Weinman, K., van der, Ven, H., Mockett, C., et al.: A study of grid convergence issues for the simulation of the massively separated flow around a stalled airfoil using DES and related methods. In: Wesseling, P., Oñate, E., Périaux, J. (eds.) European Conference on Computational Fluid Dynamics (ECCOMAS CFD). TU Delft, Niederlande (2006)

Authors and Affiliations

Axel Probst[1] · Elrawy Soliman[1] · Silvia Probst[1] · Matthias Orlt[1] · Tobias Knopp[1]

✉ Axel Probst
axel.probst@dlr.de

Elrawy Soliman
elrawy.soliman@dlr.de

Silvia Probst
silvia.probst@dlr.de

Matthias Orlt
matthias.orlt@dlr.de

Tobias Knopp
tobias.knopp@dlr.de

[1] Institute of Aerodynamics and Flow Technology, DLR (German Aerospace Center), Bunsenstrasse 10, 37073 Göttingen, Germany